9

Drift chambers

9.1 Single wire drift chambers

The possibility of measuring the electrons' drift time and getting additional information about the spatial coordinates of an ionizing event was suggested in the early works on multi-wire proportional chambers (Charpak *et al.*, 1968). In its basic form, a single-cell drift chamber has a narrow gap of constant electric field, with a wire counter at one end, Figure 9.1. Field-shaping electrodes, wires or strips, at decreasing potentials between the anode and a top drift electrode, provide the required electrical configuration. Ionization electrons released in the gas by a charged particle at a time t_0 migrate in the electric field and reach the anode wire where they are amplified and detected at a time t_1. The distance of the track from the anode wire is then obtained from $t_1 - t_0$ through the knowledge of the time–space correlation, measured or computed from the electric field map and the field dependence of drift velocity, $w = w(E)$. In the region of uniform field, the relative space coordinate is simply given by $s = w\ (t_1 - t_0)$.

Unlike MWPCs, drift chambers require a time reference signal, and can be used for the localization of charged particles exploiting an external trigger provided by one or more scintillation counters; for neutral radiation, the time reference can be obtained from the detection of the primary scintillation caused by the interaction in the gas. Albeit having reduced rate capability, due to the long electron collection time as compared to MWPCs, drift chambers permit one to reduce the number of readout channels while providing sub-mm localization accuracies, and have therefore been developed in a variety of models and widely used in experimental setups.

If a large surface of detection is required, a simple structure like the one described leads to uncomfortably large working voltages and long drift times. Nevertheless, chambers of this design reaching 50 cm drift lengths have been successfully operated, with drift voltages around 50 kV and a maximum drift time of about 10 μs (Saudinos *et al.*, 1973; Rahman *et al.*, 1981). Figure 9.2, from data

https://doi.org/10.1017/9781009291200.011 Published online by Cambridge University Press

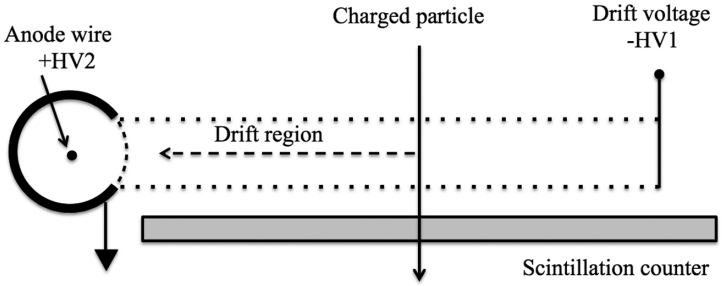

Figure 9.1 Schematic of a single-cell drift chamber.

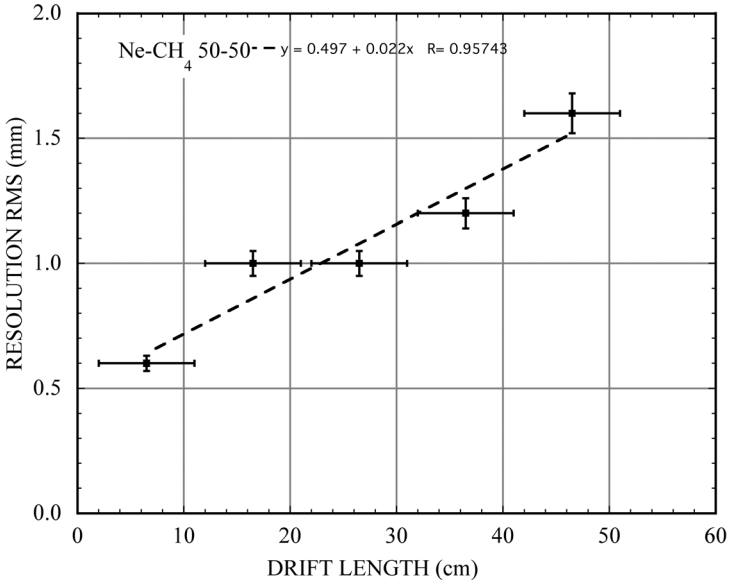

Figure 9.2 Position accuracy for a 50 cm long single cell drift chamber. Data from Saudinos *et al*., (1973).

in the first reference, shows the position accuracy of the detector as a function of drift distance; the horizontal error bars represent the region over which the measurement was averaged.

9.2 Multi-cell planar drift chambers

Multi-cell drift structures can cover larger detection areas with shorter memory times; however, since the region of the anode wire becomes part of the active volume, the drift field is not uniform across all the active cell, and the space–time correlation is necessarily distorted. A standard multi-wire proportional chamber can be used as a drift chamber; nevertheless, especially for large wire spacing,

https://doi.org/10.1017/9781009291200.011 Published online by Cambridge University Press

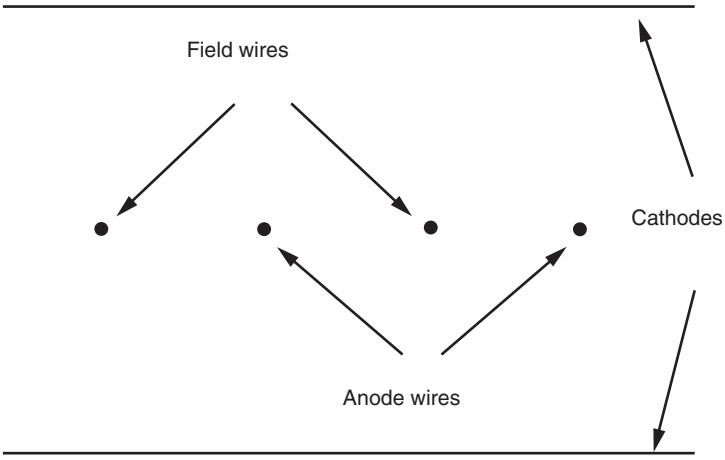

Figure 9.3 Schematics of a multi-wire drift chamber.

the presence of a low field region between the anodes results in non-linearity of the space–time relationship and can have slow electron trails at long drift times.

Introduced by H. Walenta and collaborators (Walenta *et al.*, 1971), a modification of the original MWPC structure, named the multi-wire drift chamber (MWDC) or simply drift chamber (DC) allows the reduction of low field regions in the central plane. As seen in Figure 9.3 and Figure 9.4, the anode wires alternate with thicker field wires, at suitable potentials to reinforce the electric field in the critical region. A system of drift chambers of this design, with 20 mm wire spacing and sizes up to a square metre, was successfully operated in a spectrometer experiment in the early seventies, achieving localization accuracies better than 400 μm rms (Walenta 1973). A recording of the induced signals on the field wires can be used to resolve the right–left ambiguity, intrinsic in all symmetric multi-wire structures (Walenta, 1978). Similar detectors have been built in a wide range of wire spacing and up to sizes exceeding tens of square metres (Cheng *et al.*, 1974; Bernreuther *et al.*, 1995).

The position resolution that can be achieved with multi-wire drift chambers depends on the knowledge of the space–time correlation and the intrinsic diffusion properties of migrating electrons. Due to the chamber geometry with a non-uniform electric field, the correlation is generally not linear, although an appropriate choice of the gas and operating condition can reduce the variations; the correlation depends also on the angle of incidence of the tracks. An example is shown in Figure 9.5, measured for tracks normal to a large size MWDC with 10 cm anode wire spacing (Cheng *et al.*, 1974).

Operation of the drift chambers at high pressures improves the localization accuracy, because of both the increase of ionization density and decrease in diffusion, as seen in Figure 9.6 (Farr *et al.*, 1978).

https://doi.org/10.1017/9781009291200.011 Published online by Cambridge University Press

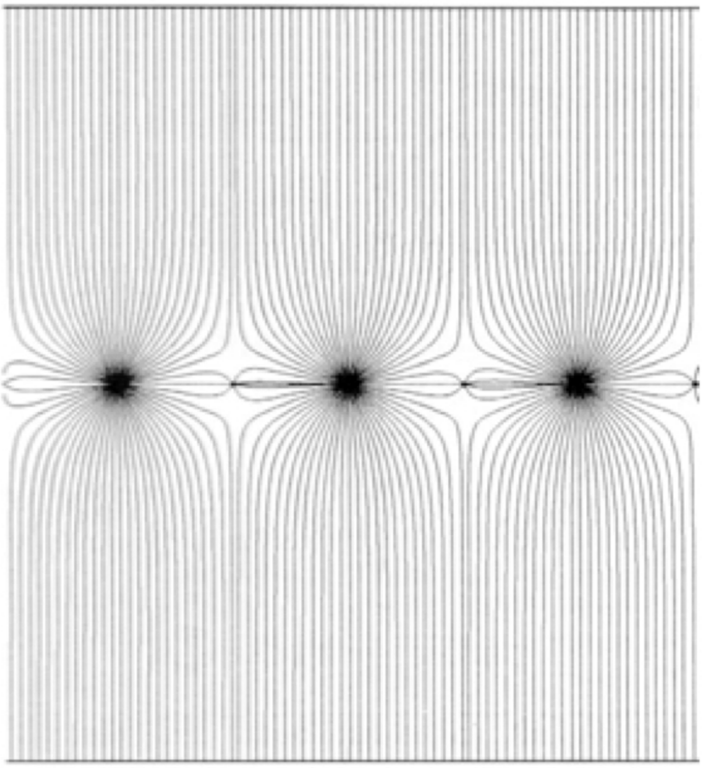

Figure 9.4 Electrical field lines in the multi-wire drift chamber.

In the presence of an external magnetic field, the electron drift lines do not coincide with the field lines, introducing distortions in the space–time correlation, which has to be measured or computed using the tools described in Chapter 4. Figure 9.7 is an example of computed drift lines and contours of constant drift times at increasing magnetic fields, parallel to the wires, and a specific choice of the gas filling and detector parameters (De Boer *et al.*, 1978).

A modification of the original MWDC, optimized to the measurement of inclined tracks and named the vertical drift chamber, is shown schematically in Figure 9.8 (Bertozzi *et al.*, 1977); the additional field wire between anodes reduces signal cross-talk between adjacent cells. A multi-cell version of this design was used for the construction of a large array of drift chambers for the L3 experiment muon detector at CERN (Becker, 1984; Viertel, 1995).

A limitation of the described design comes from the fact that, in order to obtain a relatively uniform field in the drift cells, the anode to cathode distance has to be comparable to or larger than the anode wire pitch; for the large wire spacing desirable to reduce the number of readout channels, this implies the construction of rather thick chambers, and therefore a reduced packaging density. Moreover,

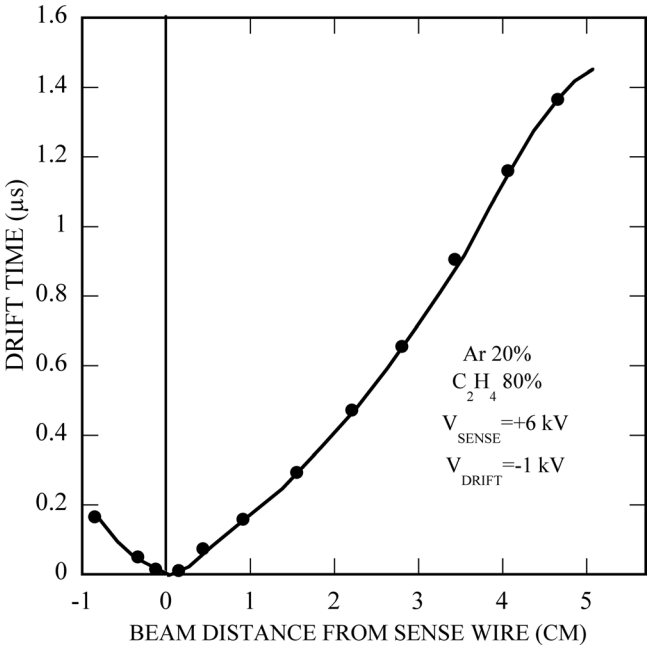

Figure 9.5 Space–time correlation in a MWDC (Cheng *et al.*, 1974). By kind permission of Elsevier.

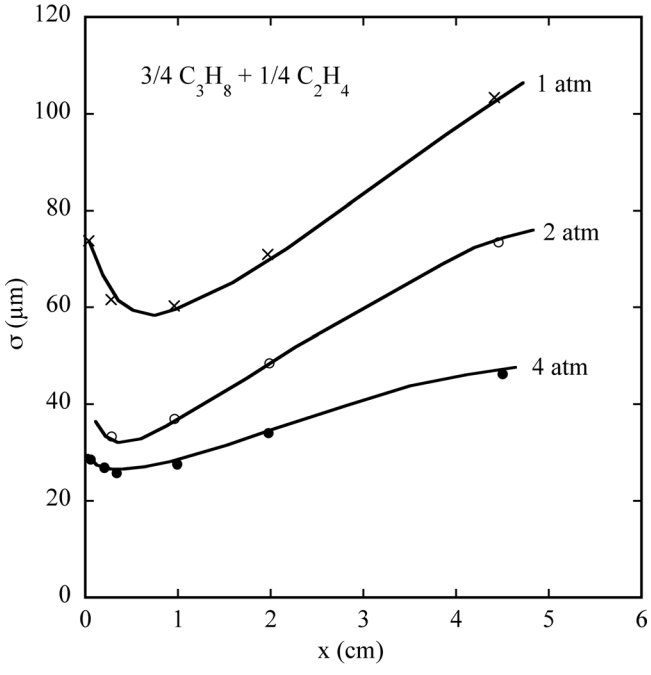

Figure 9.6 Position accuracy of a drift chamber at increasing pressures (Farr *et al.*, 1978). By kind permission of Elsevier.

https://doi.org/10.1017/9781009291200.011 Published online by Cambridge University Press

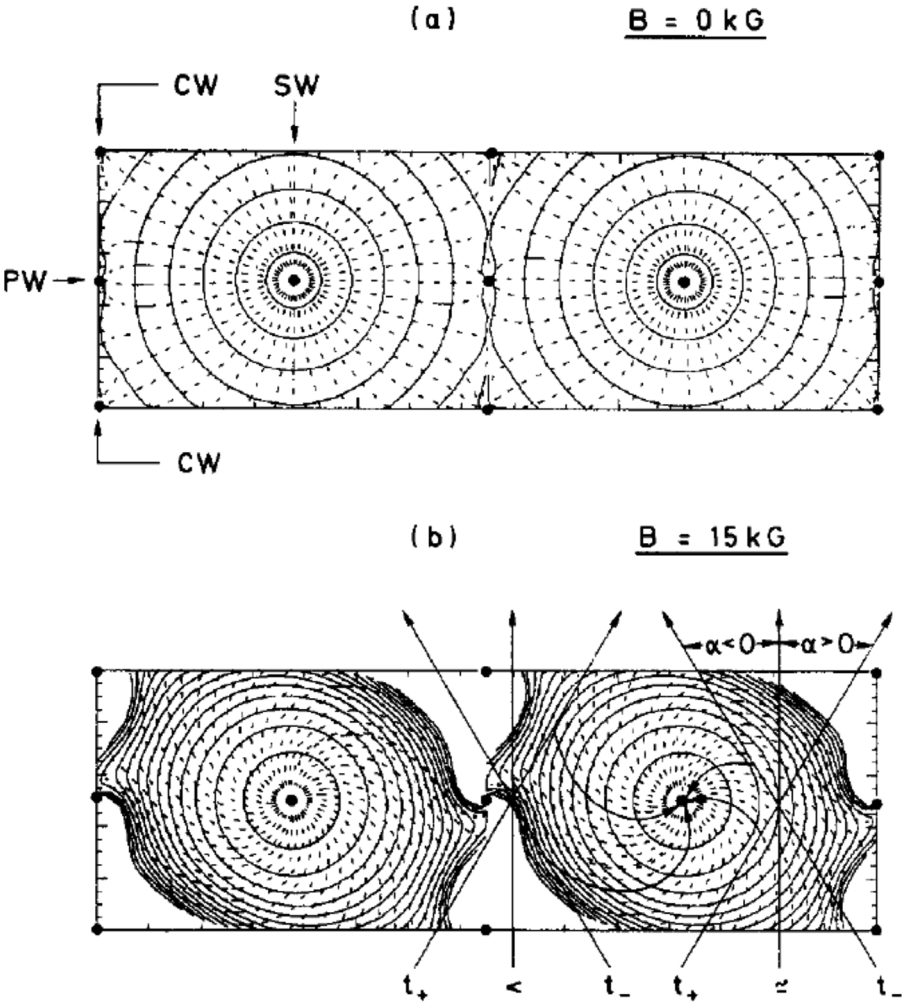

Figure 9.7 Computed electron drift lines and contours of equal drift times at increasing values of magnetic field parallel to the wires (De Boer *et al.*, 1978). By kind permission of Elsevier.

although the closest ionization electrons produce the signal used for the coordinate measurement, due to the field structure distant electrons are collected over a long time, affecting the multi-track capability.

The structure shown in Figure 9.9 (Charpak *et al.*, 1973) helps in solving both problems. Two sets of parallel cathode wire planes are connected to increasingly high negative potentials, symmetrically from the centre of the cell; the anode wire is kept at a positive potential, and additional field wires, at the potential of the adjacent cathode wires, sharpen the transition from one cell to the next. Two grounded screening electrodes protect the field structure from external influence. As shown in

https://doi.org/10.1017/9781009291200.011 Published online by Cambridge University Press

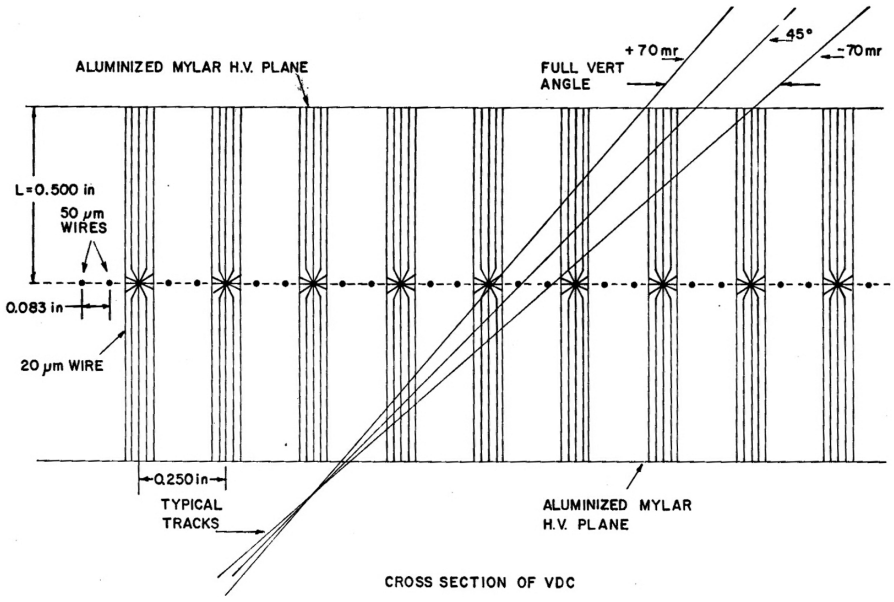

Figure 9.8 The vertical drift chamber, optimized for the detection of inclined tracks (Bertozzi *et al.*, 1977). By kind permission of Elsevier.

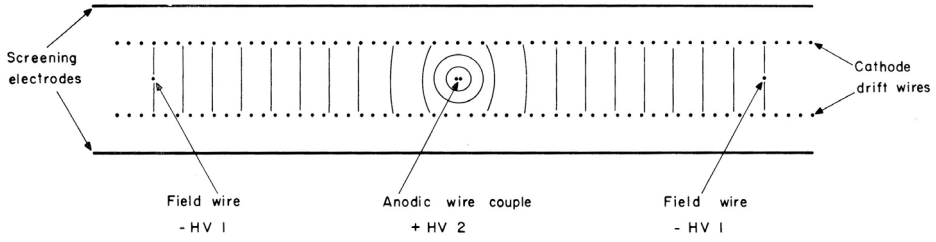

Figure 9.9 Schematics of the high accuracy drift chamber (Charpak *et al.*, 1973). By kind permission of Elsevier.

the figure, an almost equi-potential field distribution can be obtained in the median plane of the drift cell, even for gaps much narrower than the cell size; typical values of 2×3 mm and 50 mm have been used for the gaps and the anode wire spacing, respectively. An offset of the potentials applied on the two field-shaping meshes, Figure 9.10, permits one to operate in strong magnetic fields parallel to the wires, approximately compensating the Lorentz angle of the drifting electrons.

Owing to their quasi-uniform field, drift chambers of this design have a linear space–time correlation, almost independent of the incidence angle (Figure 9.11) (Breskin *et al.*, 1974b). They can achieve very good localization accuracy and multi-track resolution, and have therefore been appropriately named high-accuracy

https://doi.org/10.1017/9781009291200.011 Published online by Cambridge University Press

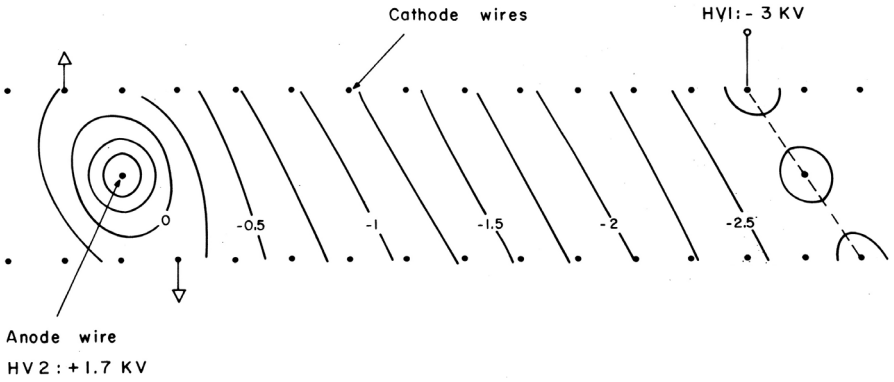

Figure 9.10 Modified equi-potentials in the high-accuracy drift chamber for operation in a magnetic field parallel to the wires (Charpak *et al.*, 1973). By kind permission of Elsevier.

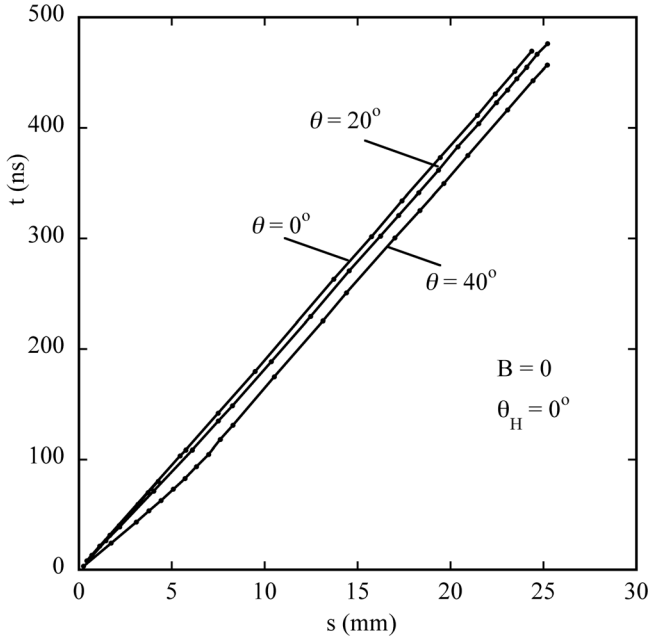

Figure 9.11 Space–time correlation in the high-accuracy drift chamber for several angles of incidence of the beam (Breskin *et al.*, 1974b). By kind permission of Elsevier.

drift chambers (HADC); an example of measured space accuracy for fast particles as a function of drift length is given in Figure 9.12 (Breskin *et al.*, 1974b). In the figure, the dashed lines show the estimated contributions of the primary ionization statistics, decreasing with the distance, of the electrons' diffusion and of the constant term due to the time measurement error.

https://doi.org/10.1017/9781009291200.011 Published online by Cambridge University Press

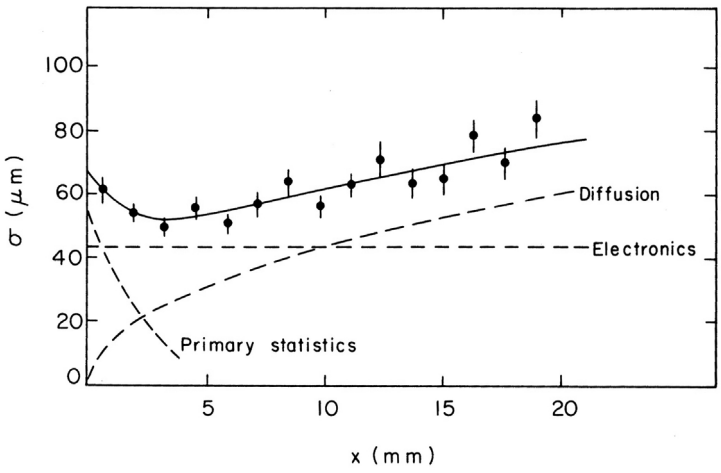

Figure 9.12 Position resolution of the HADC (points with error bars). The dashed lines show the estimated contributions of primary ionization statistics, electron diffusion and electronics (Breskin *et al.*, 1974b). By kind permission of Elsevier.

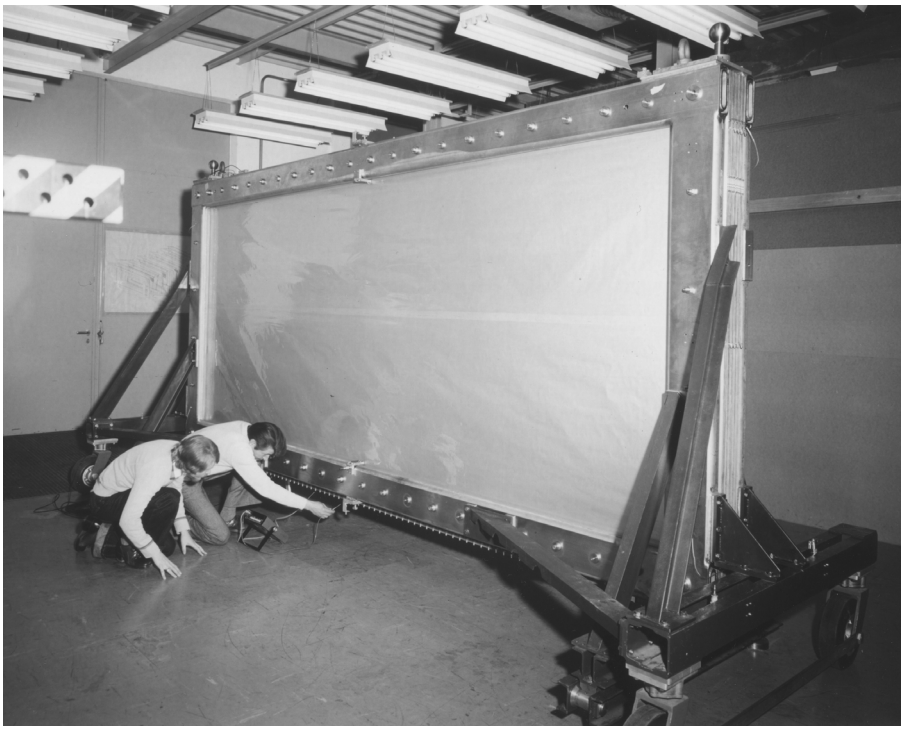

Figure 9.13 A large high-accuracy drift chamber built for the OMEGA spectrometer at CERN. Picture CERN (1976).

https://doi.org/10.1017/9781009291200.011 Published online by Cambridge University Press

Multi-cell drift chambers cannot resolve the right–left ambiguity intrinsic in their symmetric construction; the reconstruction of tracks is generally obtained using several staggered planes of measurement. A method for resolving the ambiguity locally is to separate the sensitive regions on the two sides of an anode by replacing the single wire with wire doublets, at a very short distance apart (Breskin *et al.*, 1974a). The ensuing field modification results in a small (∼1%) localized loss of efficiency for tracks perpendicular to the chamber, obliterated for inclined tracks. Due to the electrostatic repulsion between the pair, the wires have to be bonded together at short distances to avoid distortions; for the 100 μm distance used in the quoted work, droplets of epoxy 5 cm apart were used to stabilize the structure.

High-accuracy drift chambers of the described design have been used in experiments requiring single-track position resolutions of 100 μm or better, as in charged particle spectrometers (Filatova *et al.*, 1977; Chiavassa *et al.*, 1978), channeling experiments (Esbensen *et al.*, 1977) and other applications. The picture in Figure 9.13 shows the large HADC used for tracking in the Omega spectrometer at CERN; Figure 9.14 is a close view of the central wire plane under microscope

Figure 9.14 Close-up of the wire plane in the HADC. Picture CERN (1976).

https://doi.org/10.1017/9781009291200.011 Published online by Cambridge University Press

Figure 9.15 A wire plane of the large Omega drift chamber under construction. Picture CERN (1976).

inspection. Insulating garland spacers and wire supports, described in Section 8.12, were used to ensure the stability of the large structure. The picture in Figure 9.15 shows a wire plane of the chamber before assembly, with the garlands clearly visible.

Many variants of drift chamber designs have been developed to meet the requirements of large detection areas and simplified construction, aiming at large productions. Figure 9.16 is one of the early studies: metal I-beam shaped electrodes, insulated from the (grounded) cathodes and kept at negative potential, provide structural strength to the structure and permit one to reinforce the field in the middle plane of drift (Becker *et al.*, 1975). Due to charging-up and breakdown problems around the insulator's edges, this design seems to have been abandoned.

An alternative structure, also permitting a favourable gap to pitch aspect ratio is shown in Figure 9.17 (Marel *et al.*, 1977); the drift cell includes an anode and a cathode wire in the middle plane, with additional field wires kept at appropriate potentials to define the electric field structure. Grounded electrodes, fixed to honeycomb plates on both sides of the structure, ensure mechanical strength and gas tightness. Very large (4 m diameter) hexagonal-shaped drift chambers of this design were used in the eighties to instrument the WA1 neutrino experiment at CERN, Figure 9.18, and routinely achieved sub-mm localization accuracies (Holder *et al.*, 1978).

https://doi.org/10.1017/9781009291200.011 Published online by Cambridge University Press

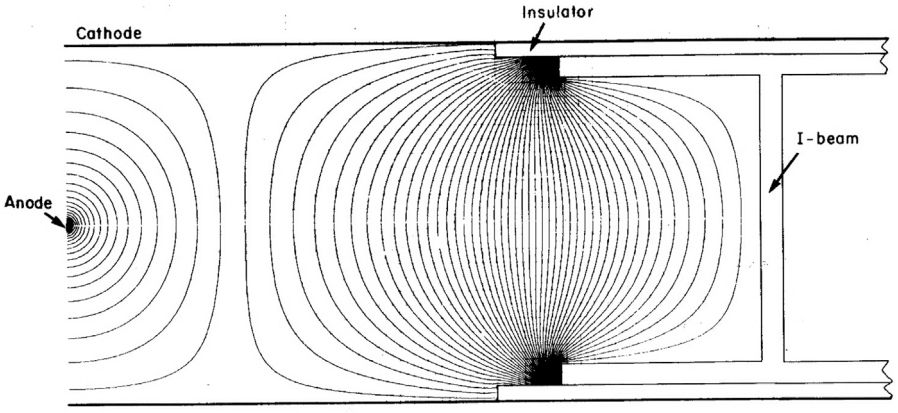

Figure 9.16 Scheme of a simple drift chamber cell with reinforcement I-beam electrodes, insulated from the cathodes, providing structural rigidity (Becker *et al.*, 1975). By kind permission of Elsevier.

Optimized for mass production, an improved design of the drift chamber described in Figure 9.16, somehow improperly named drift tube,[1] has the cell structure shown in Figure 9.19, with wires mounted between aluminium plates and I-beam profiles defining the electric field and providing mechanical stiffness (Aguilar-Benitez *et al.*, 2002; Cerminara 2010). A very large system of drift tubes has been built and operated for muon triggering, identification and tracking in the CMS barrel muon spectrometer at CERN's LHC collider; the detector is assembled in sectors around the beam, and includes 250 modules ranging between 2 and 4 m in width and 2.5 m in length (Abbiendi *et al.*, 2009).

9.3 Volume multi-wire drift chambers

The devices described above, consisting of a single plane of detection, are suitable for use in fixed target experiments such as long-arm spectrometers. Multi-cell structures have been developed to better suit the needs of experiments requiring compact detectors, particularly inside the solenoids used for magnetic analysis in storage ring colliders. Cylindrical in shape, they fill the sensitive volume with repeating cells having anodes surrounded by several field wires, and were built with a variety of schemes.

One of the first large multi-cell chambers, with simple drift cells consisting of an anode and six cathode wires, was operated for the Mark II at SLAC (Davies-White

[1] Arrays of proportional drift tubes with cylindrical cross section are described in Chapter 11.

https://doi.org/10.1017/9781009291200.011 Published online by Cambridge University Press

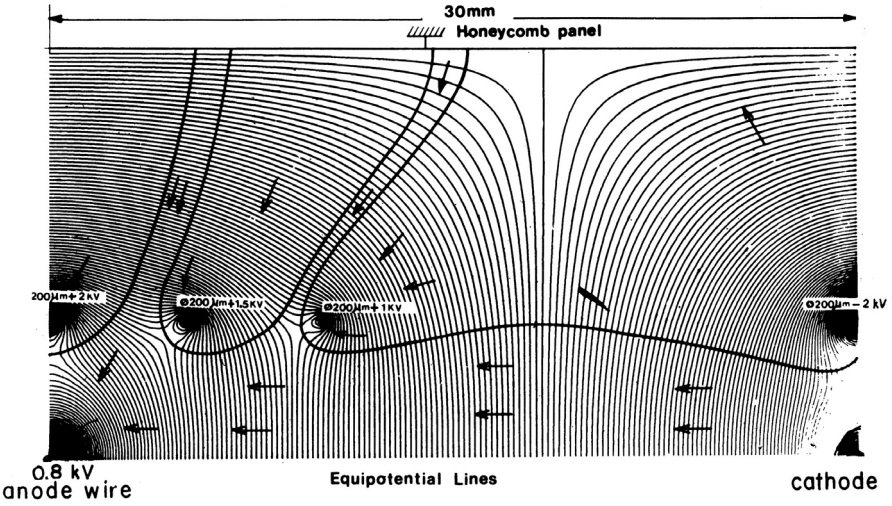

Figure 9.17 Schematics of the drift cell developed for the WA1 large drift chambers (Marel *et al*., 1977). By kind permission of Elsevier.

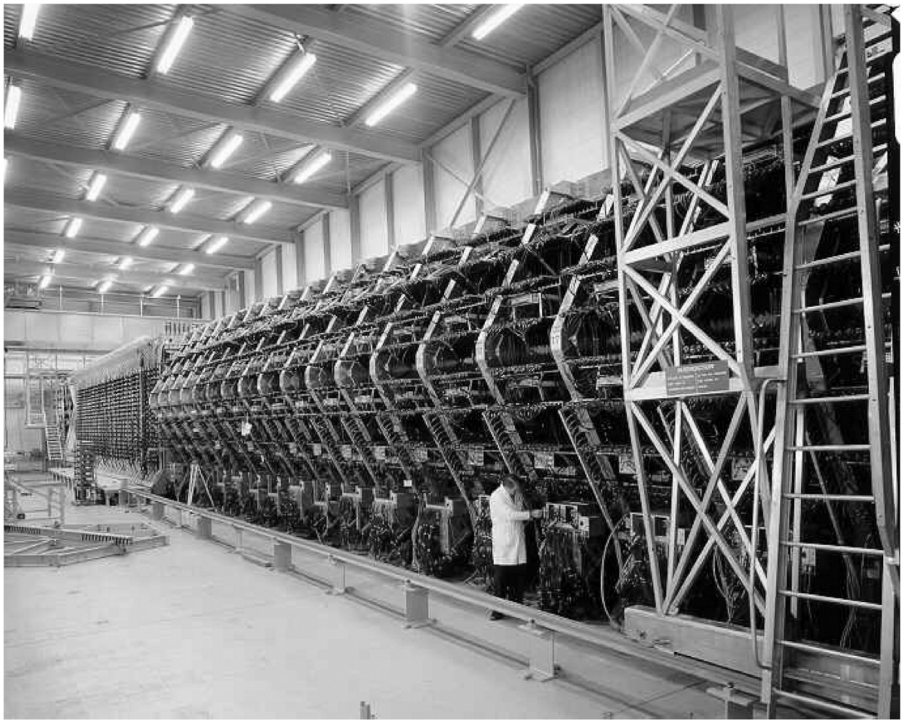

Figure 9.18 The WA1 neutrino experiment; large hexagonal drift chambers alternate with scintillators and converters. Picture CERN (1976).

https://doi.org/10.1017/9781009291200.011 Published online by Cambridge University Press

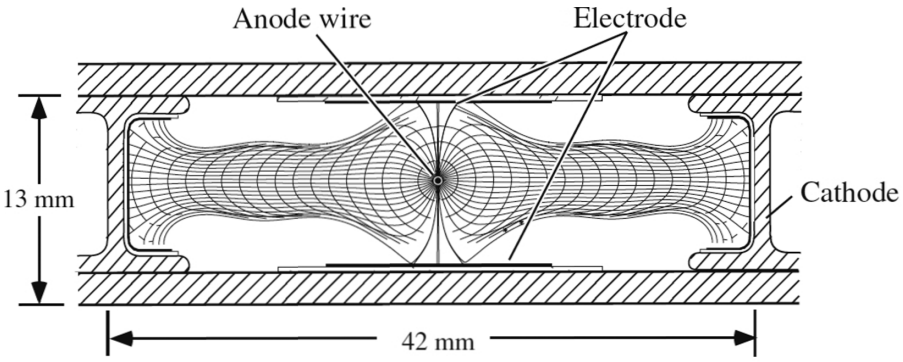

Figure 9.19 Mechanical structure and electric field in a drift tube cell (Aguilar-Benitez *et al*., 2002). By kind permission of Elsevier.

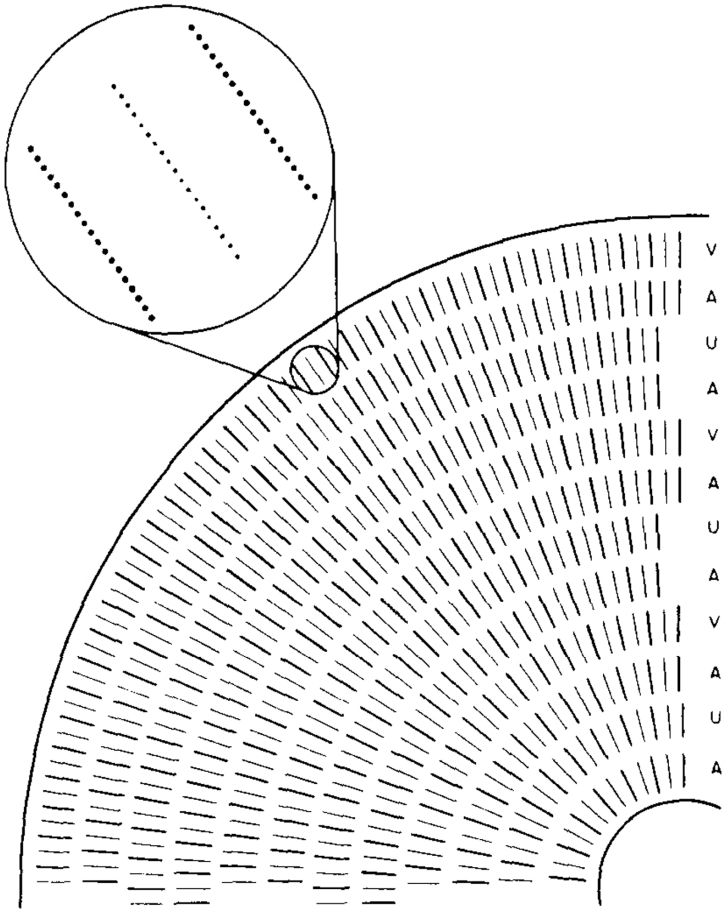

Figure 9.20 Schematics of the Mark II cylindrical drift chamber; the inset shows the cell structure (Hanson 1986). By kind permission of Elsevier.

https://doi.org/10.1017/9781009291200.011 Published online by Cambridge University Press

Figure 9.21 A cylindrical drift chamber in construction for the MARK II detector. Picture courtesy SLAC (1977).

et al., 1972), and upgraded later with a new design having the geometry shown in Figure 9.20 (Hanson, 1986). Concentric cylindrical layers with cathode wires and alternating anode and field wires fill the cylindrical volume between an inner and an outer radius; the wires are strung and stretched between two disk-shaped end-plates and soldered or crimped to the supports. The picture in Figure 9.21 shows one such chamber in construction at SLAC, with the wires hand-strung in successive layers. Figure 9.22 is a similar device built for the VENUS experiment for the TRISTAN storage ring at KEK (Arai *et al.*, 1983); in this case, the detector is assembled vertically, exploiting gravity to stretch the wires between the top and bottom end-plates.

In the presence of a magnetic field parallel to the wires, the electron drift lines are distorted as shown in the example of Figure 9.23, computed for the Mark II detector at 0.45 T; the track reconstruction requires then thorough calibrations or calculations to supply the appropriate space–time correlations (Abrams *et al.*, 1989).

With a different approach, aimed at improving performances and reliability, the UA1 central detector at CERN was an assembly of 40 drift chamber modules with the geometry shown in Figure 9.24 and Figure 9.25 (Baranco Luque *et al.*, 1980; Beingessner *et al.*, 1987). With a simultaneous recording of the track's drift time

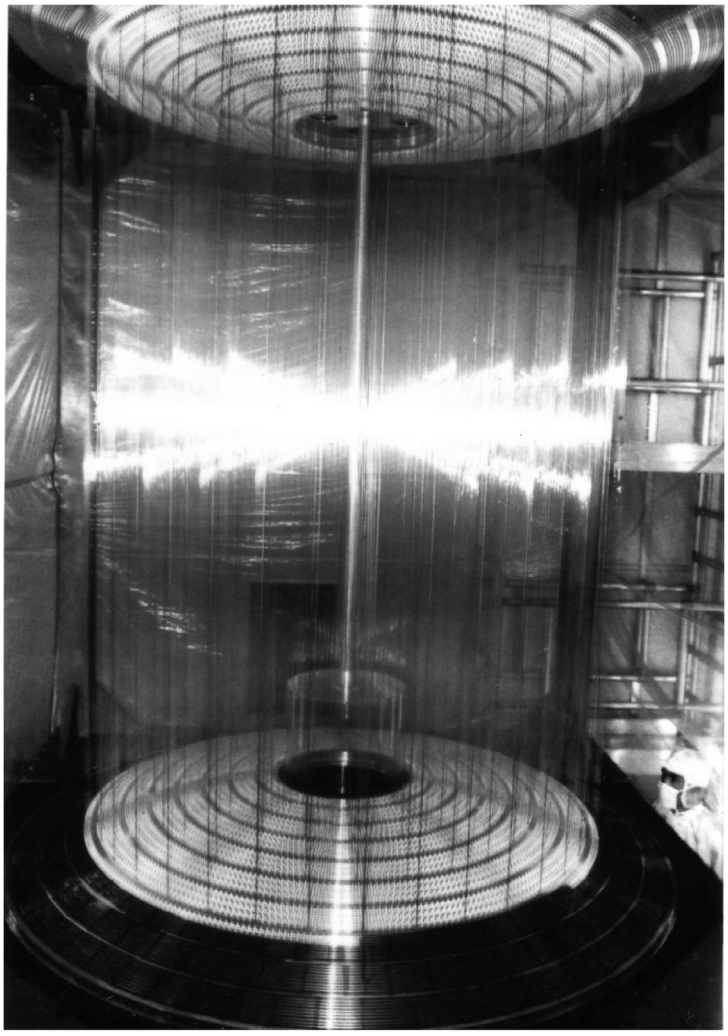

Figure 9.22 A cylindrical multi-cell drift chamber in construction at KEK (Arai *et al.*, 1983). By kind permission of Elsevier.

and of the longitudinal coordinate from the ratio of pulse heights on the two ends of the wires, and making use of a colour display visualization, innovative at the time, the detector provided amazing three-dimensional views of the events, and was appropriately named the imaging chamber. The UA1 experiment led to the discovery of the W and Z heavy bosons, and to the assignment of the 1984 Nobel Prize to Carlo Rubbia and Simon van der Meer; Figure 9.26 is the display of a W event, recorded with the drift chambers complex.

https://doi.org/10.1017/9781009291200.011 Published online by Cambridge University Press

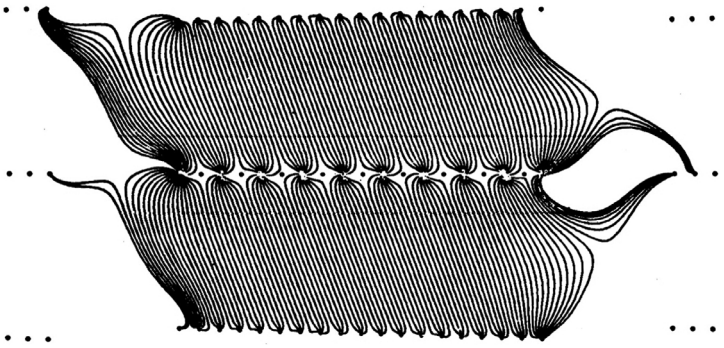

Figure 9.23 Electron drift lines in the Mark II cylindrical drift chamber in 0.45 T magnetic field parallel to the wires (Abrams *et al.*, 1989). By kind permission of Elsevier.

Similar structures have been built for many other experiments; for a summary of detectors and a comparative discussion of performances see Heintze (1978); Walenta (1983); Va'vra (1986a); Saxon (1988); Blum and Rolandi (1993).

9.4 Jet chambers

With a cylindrical geometry optimized for the detection of multiple tracks, the jet chamber (so named from the physical processes under investigation) has the structure shown in Figure 9.27 (Drumm *et al.*, 1980). Segmented radial sectors, in three consecutive shells, have a central wire plane with alternating anode and field wires, and field-shaping cathode walls to provide a near uniform electric field in the drift regions. The right–left ambiguity, intrinsic in the drift time measurement, is resolved by staggering by 150 μm the anode wires alternatly right and left from the median plane; a measurement of the charge sharing between the two ends of each wire provides the longitudinal coordinate.

The computed electron drift trajectories and equal time lines for a cell, in the presence of a longitudinal magnetic field, are shown in Figure 9.28. The detector has been operated for many years in the JADE experiment on the electron–positron storage ring PETRA at DESY, consistently providing single-track radial position accuracies between 150 and 200 μm and around 10 mm along the wires (Heintze, 1982).

A larger jet chamber of similar conception, but with a single shell of radial sectors, was operated in the OPAL experiment at CERN's LEP electron–positron collider (Fischer *et al.*, 1989), achieving intrinsic radial coordinate resolutions

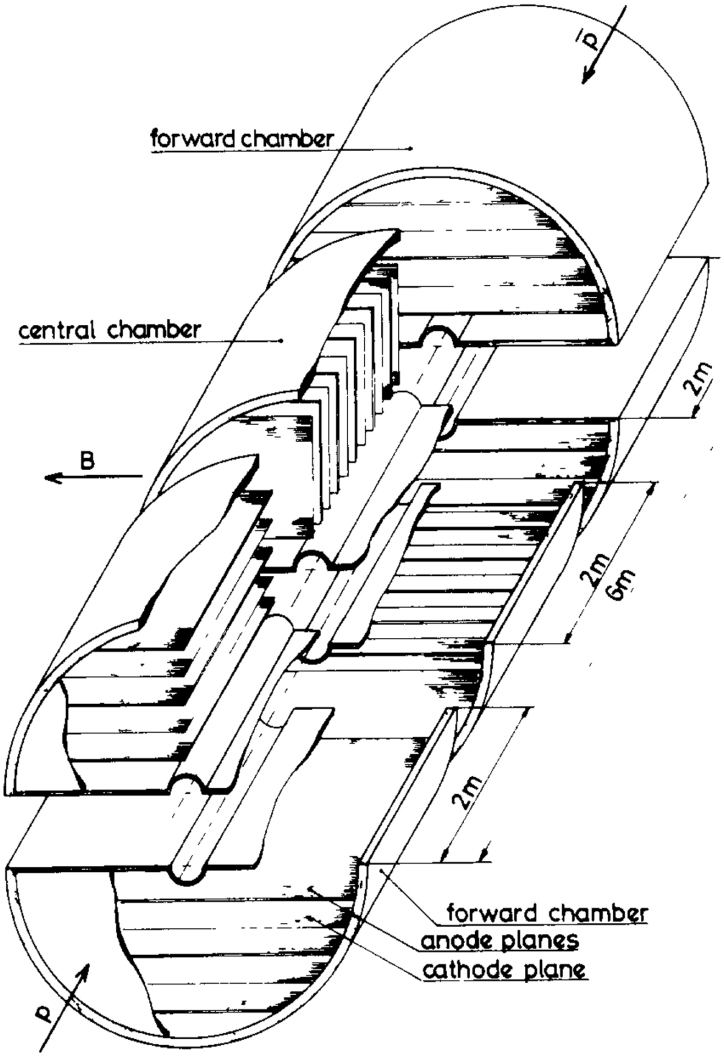

Figure 9.24 Assembly of drift chamber modules in the UA1 detector (Baranco Luque *et al*., 1980). By kind permission of Elsevier.

between 100 and 200 μm, depending on drift distance, and an overall momentum resolution of ~7% for particles around 50 GeV/c (Biebel *et al*., 1992). The picture in Figure 9.29 shows the detector under construction, and Figure 9.30 shows a recorded hadronic Z_0 decay event.

Smaller cylindrical devices of similar design have been developed as vertex detectors; operated at pressures higher than atmospheric, they can reach localization accuracies of 50 μm or better (Mμller, 1986; Alexander *et al*., 1989).

https://doi.org/10.1017/9781009291200.011 Published online by Cambridge University Press

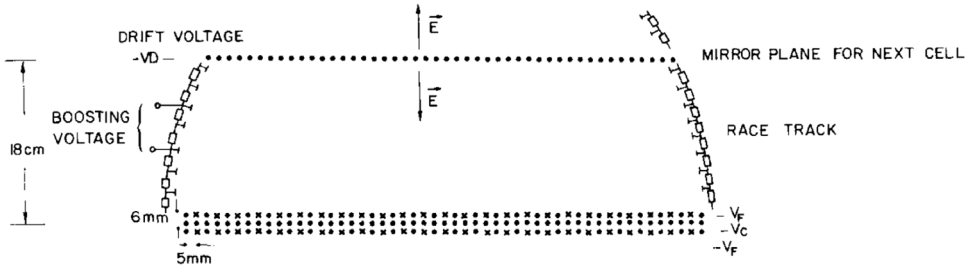

Figure 9.25 Cross section of the UA1 drift chamber module (Baranco Luque *et al*., 1980). By kind permission of Elsevier.

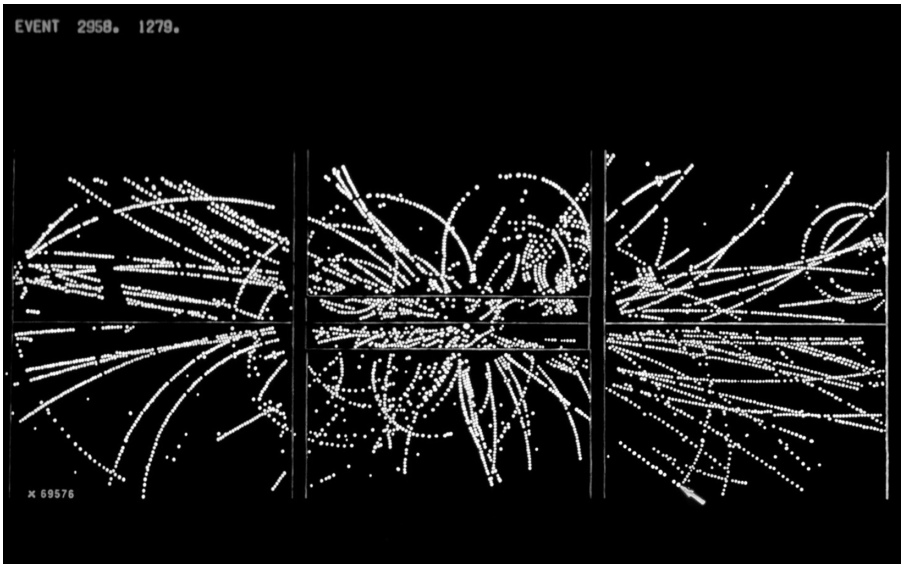

Figure 9.26 On-line display of a W event, recorded with the UA1 drift chamber system. Picture CERN (1984).

9.5 Time expansion chamber

The ultimate limit in localization properties of a drift chamber depends on two major factors: the diffusion properties of electrons, with the ensuing statistical dispersion of the single cluster collection time, and the resolution of the electronics used to record the drift time. The time expansion chamber (TEC) (Walenta, 1979), with the electrode arrangement shown in Figure 9.31, is based on the choice of a field value and a gas with low diffusion and low drift velocity to reduce the error given by the electronics' resolution. As in general diffusion decreases with field while drift velocity increases, the somewhat conflicting requirements are best met in some 'cool' gas mixtures; one example is shown in Figure 9.32 for a carbon

https://doi.org/10.1017/9781009291200.011 Published online by Cambridge University Press

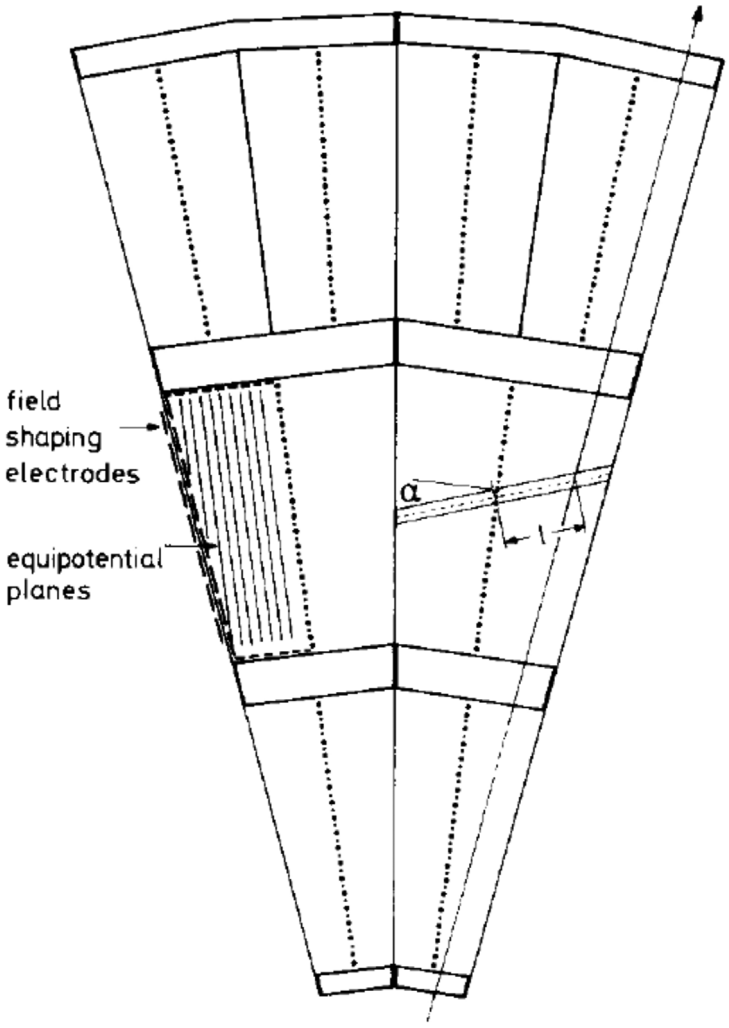

Figure 9.27 Cross section of two sectors in the JADE jet chamber (Drumm *et al.*, 1980). By kind permission of Elsevier.

dioxide–isobutane mixture, used for most the TEC developments (Commichau *et al.*, 1985). At fields around 600 V/cm, the single electron diffusion is 50 μm for 1 cm of drift, and the drift velocity 5 μm/ns, about a factor of ten lower than for a standard, saturated drift chamber gas; this corresponds to an intrinsic electronic resolution of 5 μm for a 1 ns time recording accuracy.

With a cylindrical multi-sector construction, TEC-based vertex detectors have been operated in the L3 experiment at CERN's large electron–positron collider (LEP) (Adeva *et al.*, 1990; Akbari *et al.*, 1992; Anderhub *et al.*, 2003) and the

https://doi.org/10.1017/9781009291200.011 Published online by Cambridge University Press

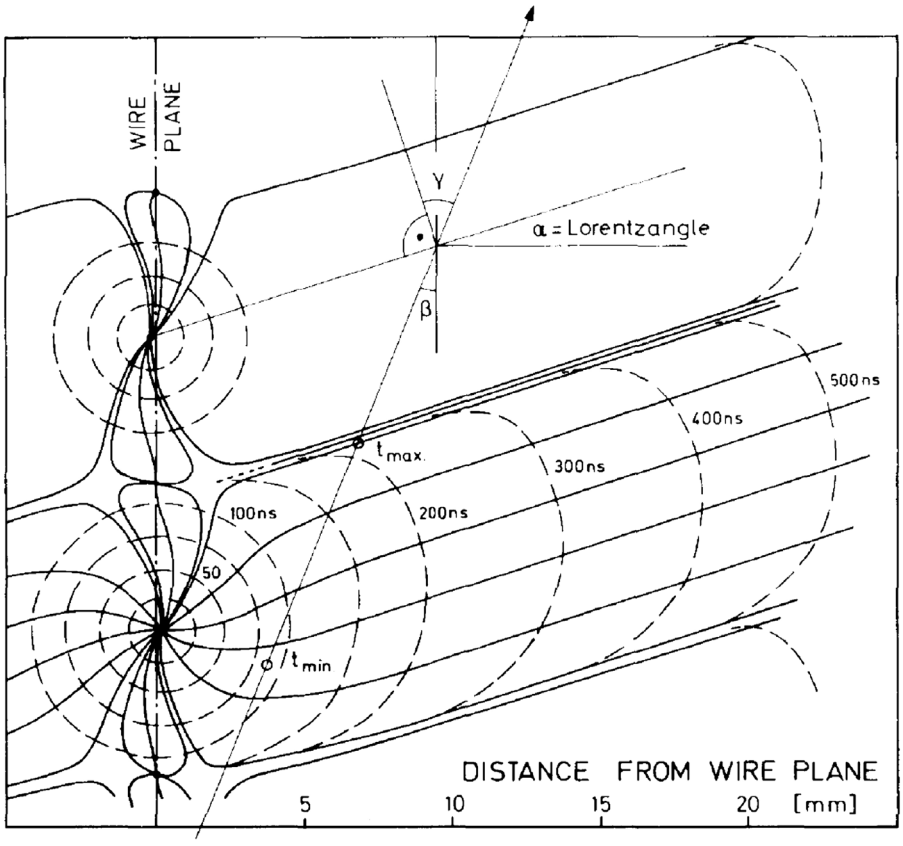

Figure 9.28 Computed electron drift trajectories and equal time lines in the jet chamber in a longitudinal magnetic field of 0.45 T (Drumm *et al.*, 1980). By kind permission of Elsevier.

Mark J detector at DESY (Anderhub *et al.*, 1986). Figure 9.33 and Figure 9.34 show, respectively, a recorded event and the single-track position resolution in the radial coordinate measured with the L3 vertex detector (Akbari *et al.*, 1992).

While satisfactorily operating at moderate particle rates, concerns about the ageing properties of hydrocarbon-based gases have suggested in later applications the use of the non-polymerizing dimethyl-ether (DME) as gas filling (Hu *et al.*, 2006). Due to the use of a non-saturated drift velocity, a good knowledge of the dependence of drift time on temperature and pressure and thorough monitoring of the ambient conditions are needed for long-term operation.

9.6 Determination of the longitudinal coordinate from current division

Drift chambers of the various designs described above provide only one coordinate, albeit with great accuracy. For unambiguous track reconstruction, particularly

https://doi.org/10.1017/9781009291200.011 Published online by Cambridge University Press

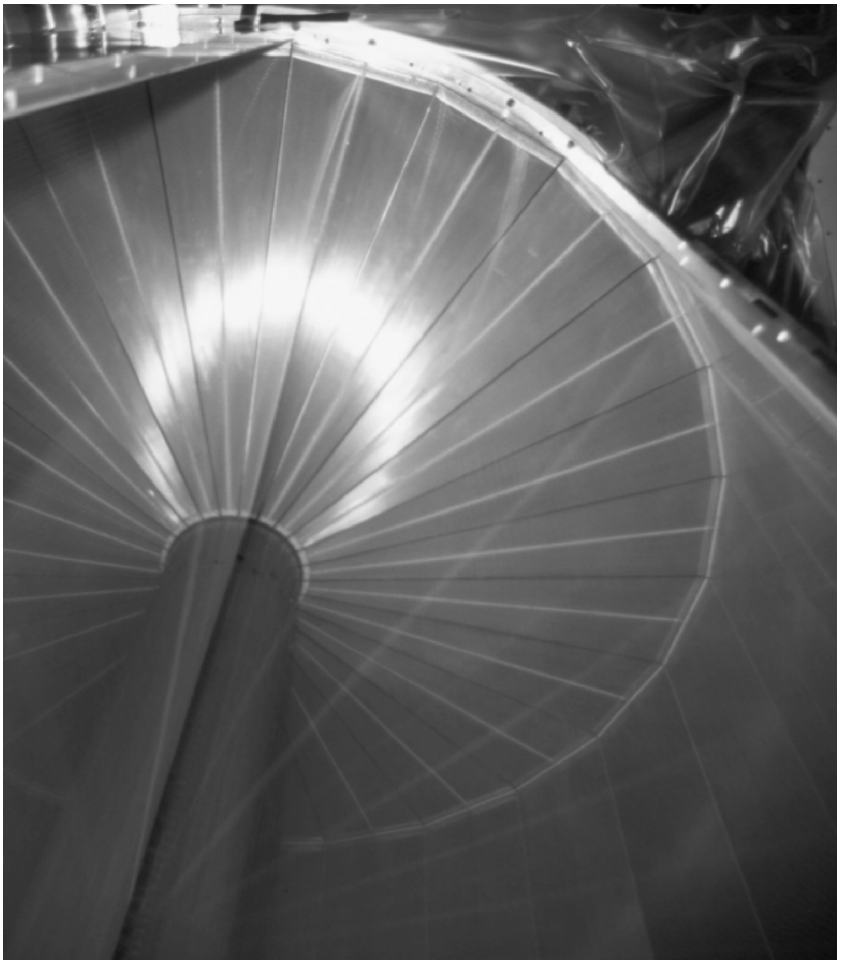

Figure 9.29 The OPAL jet chamber in construction. Picture CERN (1988).

in the case of high multiplicities, a second coordinate along the wires is desirable and in some cases, as for cylindrical devices, indispensable; the methods described in the previous chapter based on signal pickup on electrodes facing the anodes are generally not possible.

The longitudinal coordinate can be obtained from a measurement of the charge at one or both ends of a wire, exploiting the attenuation due to its resistivity, a method used already for triggered spark chambers (Charpak *et al.*, 1963) and single-wire proportional counters (Kuhlmann *et al.*, 1966; Miller *et al.*, 1971).

For a wire of linear resistivity ρ and length l, the currents detected at the two ends on equal loads R for a charge generated at position x are:

https://doi.org/10.1017/9781009291200.011 Published online by Cambridge University Press

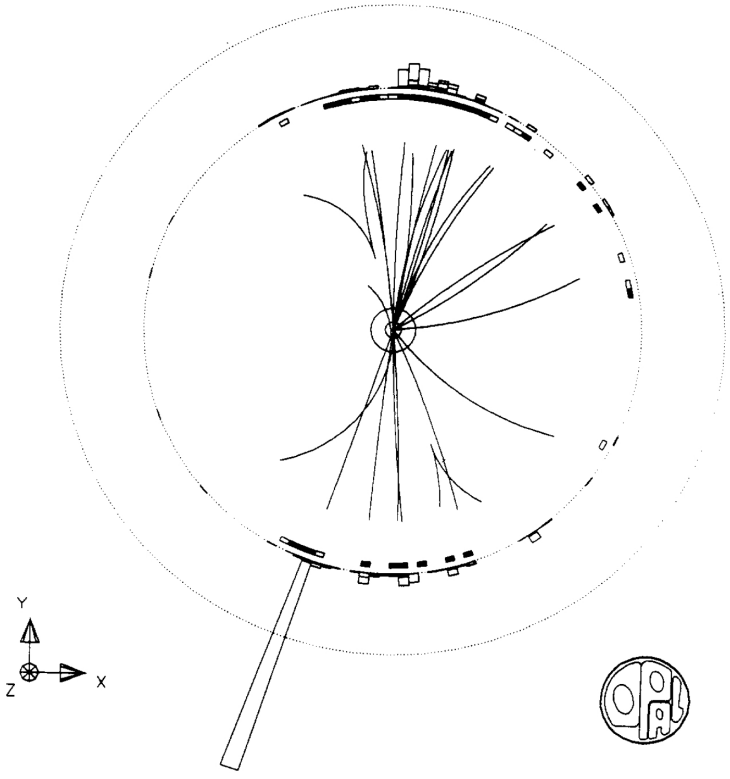

Figure 9.30 A Z_0 decay event recorded with the OPAL jet chamber; the polygons on the outer shell represent the response of the calorimeter (Baines *et al*., 1993). By kind permission of Elsevier.

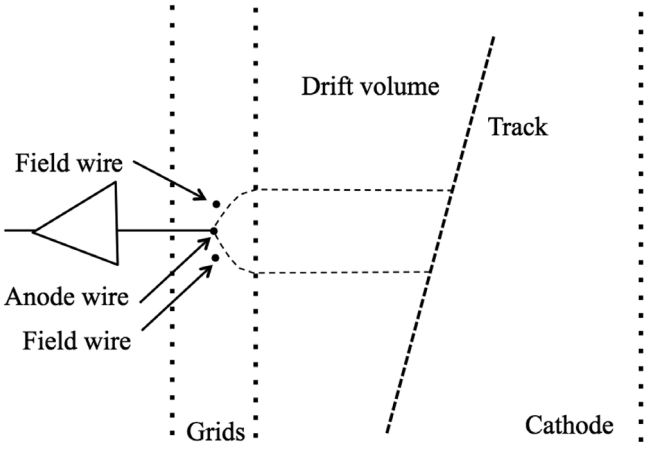

Figure 9.31 Schematics of the time expansion chamber (Commichau *et al*., 1985). By kind permission of Elsevier.

https://doi.org/10.1017/9781009291200.011 Published online by Cambridge University Press

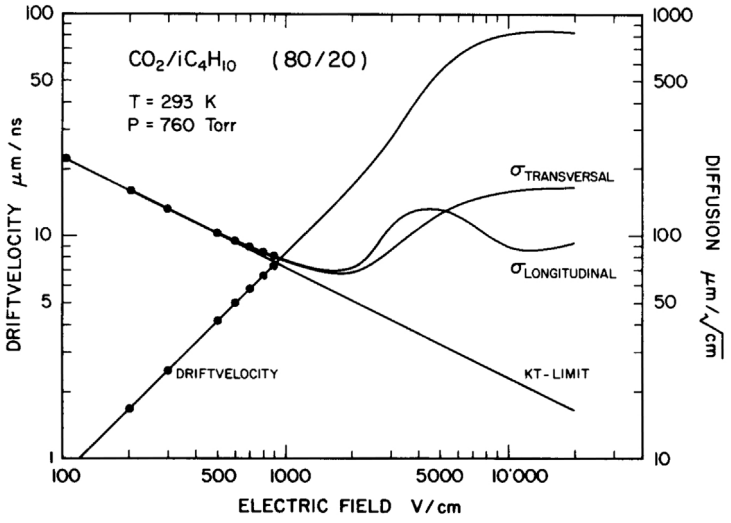

Figure 9.32 Electron drift velocity and diffusion as a function of electric field in a CO_2-iC_4H_{10} 80–20 mixture at STP (Commichau *et al.*, 1985). By kind permission of Elsevier.

$$I_1 = I_0 \frac{1 + (l - x)\rho/R}{2 + l\rho/R} \text{ and } I_2 = I_0 \frac{1 + x\rho/R}{2 + l\rho/R},\ I_0 = I_1 + I_2.$$

A more general formulation that takes into account unequal amplifier impedances and gains is given in Buskens *et al.* (1983).

The position determination achievable with the current division method depends on the resistivity of the anode wire used; with a standard gold-plated tungsten wire 20 μm in diameter ($\rho = 1.8\ \Omega$.cm) an accuracy of around 4 mm rms, or ∼1% of the wire length, could be obtained (Charpak *et al.*, 1973); better localization can be obtained using higher resistivity wires (Bouclier *et al.*, 1898; Foeth *et al.*, 1973; Fischer *et al.*, 1976; Ford 1979; Biino *et al.*, 1988).

Longitudinal localization by current division has been used successfully in many large volume drift chamber systems described in the previous sections: the UA1 vertex detector (Beingessner *et al.*, 1987) and the JADE and OPAL jet chambers (Heintze, 1982; Biebel *et al.*, 1992).

9.7 Electrodeless drift chambers

A curious variation of the basic drift chamber design has been developed, in which the field needed to drift the electrons is not shaped by additional electrodes, but by the charges deposited on insulating surfaces constituting the detector walls (Allison *et al.*, 1982). Named wireless drift tubes or electrodeless drift chambers, the

https://doi.org/10.1017/9781009291200.011 Published online by Cambridge University Press

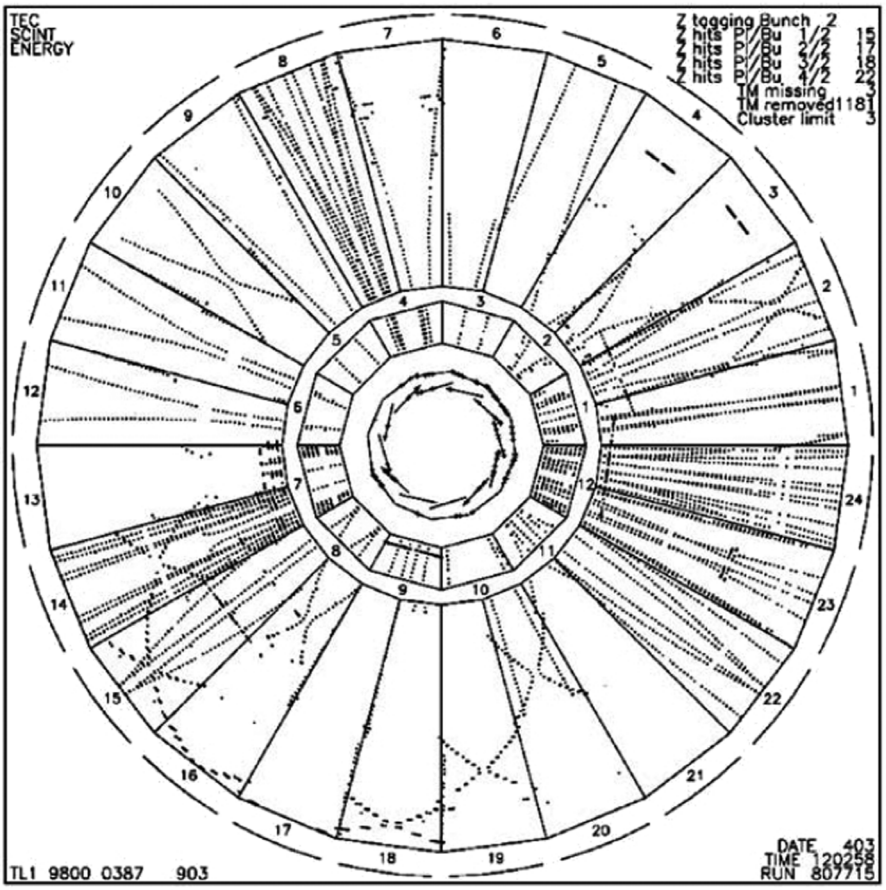

Figure 9.33 An electron–positron collision event recorded with the L3 TEC at LEP (Akbari *et al.*, 1992). By kind permission of Elsevier.

devices exploit a fundamental property of electrostatics: charges created by ionization or avalanche processes in the gas deposit on insulating surfaces with a distribution that tends to oppose further depositions, the equilibrium being reached when all field lines are made parallel to the insulator surfaces. Figure 9.35 (Zech, 1983) shows schematically the field build-up process; this in principle allows the construction of drift tubes of arbitrary shape and length.

Resulting from a dynamic equilibrium condition, the field shaping process depends on the charge production rate and distribution, and needs a 'formation' time before the counter becomes operational. These processes have been studied in detail for different detector geometry, demonstrating that reasonably high and stable efficiencies can be reached at moderate particle fluxes (Dörr *et al.*, 1985;

https://doi.org/10.1017/9781009291200.011 Published online by Cambridge University Press

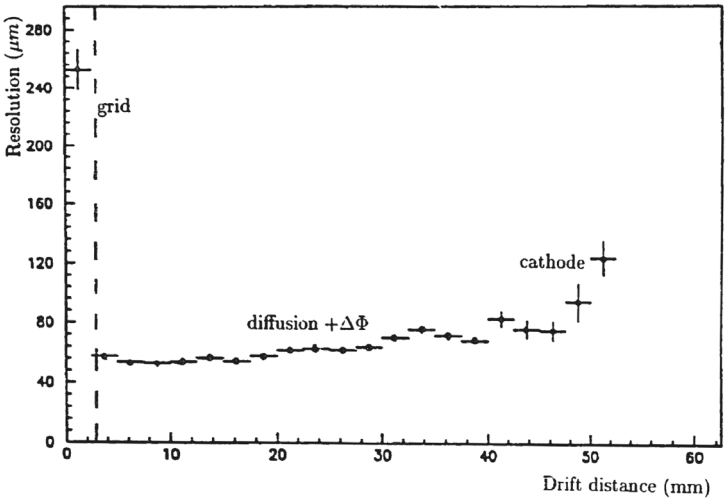

Figure 9.34 Space accuracy as a function of distance from the anode measured with the L3 TEC detector (Akbari *et al.*, 1992). By kind permission of Elsevier.

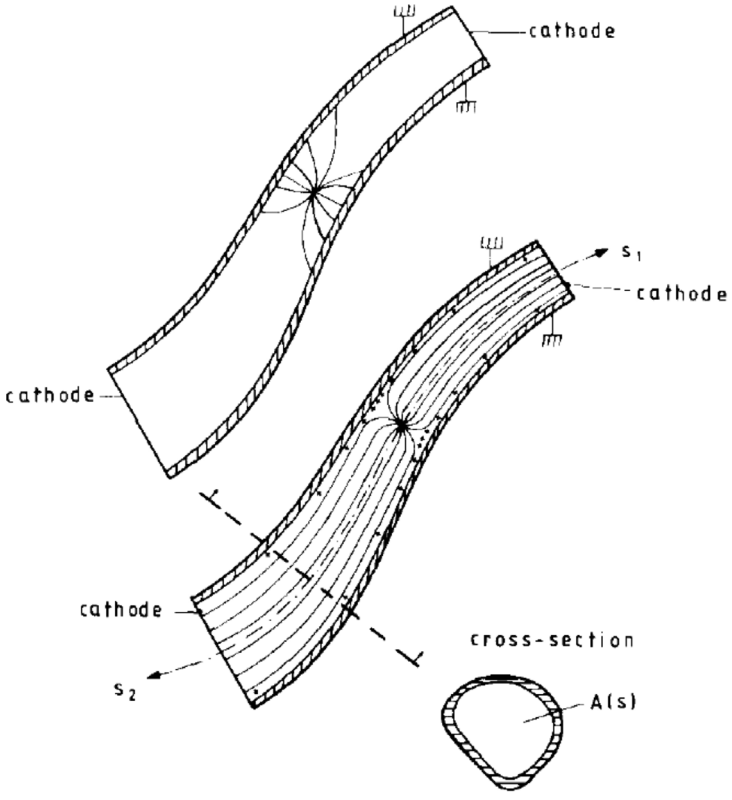

Figure 9.35 Schematics of the field-shaping build-up in the electrodeless drift tube (Zech, 1983). By kind permission of Elsevier.

https://doi.org/10.1017/9781009291200.011 Published online by Cambridge University Press

Budagov *et al*., 1987). Although the devices had only limited applications, some of the results of this work have been exploited in the development of plastic streamer tubes (see Chapter 11), and are often invoked to explain bizarre behaviours of detectors having insulators near the active electrodes.

9.8 General operating considerations

Drift chambers are, in general, easier to operate than multi-wire proportional chambers, due to the large anode wire spacing; most considerations on multiplication factors and gas choice described in the previous chapter apply as well with the necessary modifications due to the geometry. Gas purity is, of course, of primary importance, especially if long drift spaces are used. The effect of electro-negative gas pollution has been discussed in Section 4.8; common practice has shown that commercial grade purities are sufficiently good for moderate drift lengths, up to a few cm, but the gas tightness of the chamber and of the tubing have to be carefully checked and continuously monitored in long-standing experiments.

It should be emphasized that the good values of accuracy given in the examples of Figure 9.6 and Figure 9.12 are the result of local measurements, realized generally with short beam exposures. To preserve the accuracies in an actual experiment, one has to know precisely the local space–time correlations, which can be affected by the electric field strength and direction, atmospheric pressure, gas composition and temperature, external factors modifying the drift properties (electric or magnetic stray fields), and mechanical imperfections. Although it is in principle possible to take all these factors into account by calibration and monitoring, for a realistic system it is more reasonable to define limits to the tolerable variations, as a function of the desired final accuracy. The choice of a gas with drift velocity saturation decreases the dependence on the reduced electric field E/P and on temperature, as discussed in Section 4.7. The dependence on gas composition is also reduced at saturation, and has been measured in the gas mixture used in the high-accuracy drift chambers (Breskin *et al*., 1974b): to maintain a ± 50 μm stability over 25 mm of drift, a maximum temperature variation of ± 7 ^{0}C and gas composition changes of $\pm 1.6\%$ should be assured.

Mechanical tolerances and electrostatic deformations contribute directly to the factors limiting accuracy; for large chambers the thermal expansion of the materials should also be taken into account.

9.9 Drift chamber construction

As for the multi-wire proportional chambers, only a brief mention is given here on the construction of drift chambers, and the reader is referred to the quoted

literature for more information. Basically, the same techniques developed for the construction of proportional chambers have been used for drift chambers.

Calculation of the electrostatic forces in a chamber with a structure like the one in Figure 9.8 is relatively straightforward and shows that anodic instabilities do not appear for commonly used lengths of the wires, owing to the larger wire distance and diameter (Cheng *et al.*, 1974). On the other hand, the two cathode planes are attracted inwards and the overall deformation can be estimated following the methods outlined in Section 8.12. For the more complex high accuracy drift chamber (Figure 9.9) the critical elements are the field wires: since the adjacent cathode wires have a charge equal in sign, they are subjected to an outward force. Gap-restoring strip inserted at intervals between the cathodes and the screening electrodes, visible in Figure 9.15, have proved to be sufficient to compensate the electrostatic forces; external to the active volume of the chamber, the strips do not affect the performance of the drift chamber.

Further reading

Palladino, V. and Sadoulet, B. (1975) Applications of classical theory of electrons in gases to drift proportional chambers. *Nucl. Instr. and Meth.* **128**, 323.

Blum, W. and Rolandi, G. (1993) *Particle Detection with Drift Chambers* (Berlin, Springer-Verlag).